



# Thermal design and management of micro-pin fin heat sinks for energy-efficient three-dimensional stacked integrated circuits

Daewoong Jung<sup>a</sup>, Haeun Lee<sup>a,b</sup>, Daeyoung Kong<sup>a,b</sup>, Eunho Cho<sup>a</sup>, Ki Wook Jung<sup>c</sup>, Chirag R. Kharangate<sup>d</sup>, Madhusudan Iyengar<sup>e</sup>, Chris Malone<sup>e</sup>, Mehdi Asheghi<sup>c</sup>, Kenneth E. Goodson<sup>c</sup>, Hyounghoon Lee<sup>a,b,\*</sup>

<sup>a</sup> School of Mechanical Engineering, Chung-Ang University, Seoul 06974, Republic of Korea

<sup>b</sup> Department of Intelligent Energy and Industry, Chung-Ang University, Seoul, 06974, Republic of Korea

<sup>c</sup> Department of Mechanical Engineering, Stanford University, Stanford, CA 94305, USA

<sup>d</sup> Mechanical and Aerospace Engineering Department, Case Western Reserve University, Cleveland, OH 44106, USA

<sup>e</sup> Google LLC, Mountain View, CA 94043, USA

## ARTICLE INFO

### Article history:

Received 31 October 2020

Revised 31 January 2021

Accepted 28 February 2021

Available online 9 May 2021

### Keywords:

3D integrated circuit  
thermal management  
micro-pin fin array  
heat transfer  
pressure drop  
thermal performance index

## ABSTRACT

Three-dimensional stacked electronics have substantially improved the electrical performance of integrated circuits. However, given the geometrical complexity and high pressure drop they entail, thermal management difficulties and energy requirements are exacerbated owing to the inapplicability of thermal management schemes. In this study, the thermal and hydrodynamic characteristics of various micro-pin fin arrays were investigated to maximize heat dissipation while minimizing the energy consumption. Specifically, a  $10 \times 10 \text{ mm}^2$  micro-pin fin array was fabricated on an eight-inch silicon wafer via microfabrication. A Pyrex cover was bonded anodically with the top side of the micro-pin fins to prevent leakage, and a titanium/gold thin film serpentine heater was used to supply uniform heat flux on the backside of the micro-pin fin array. Subsequently, the heat transfer and pressure drop in the micro-pin fin heat sinks were obtained experimentally with various micro-pin fin geometries having pin diameter  $D_f = 38\text{--}100 \text{ }\mu\text{m}$ , transverse pin spacing  $S_T = 74\text{--}301 \text{ }\mu\text{m}$ , longitudinal pin spacing  $S_L = 74\text{--}301 \text{ }\mu\text{m}$  and pin height  $H_f = 90\text{--}207 \text{ }\mu\text{m}$ . Thereafter, the geometrical and operational effects on heat transfer and pressure drop were investigated based on a consolidated database cumulated from the literature. Altogether, 256 data points from 21 geometrical combinations were explored from existing relevant studies to obtain optimized geometric and operating conditions in the micro-pin fin arrays over a wide range of geometrical and operating conditions: Reynolds number  $Re = 35\text{--}491.3$ , heat flux  $q'' = 0\text{--}114 \text{ W/cm}^2$ , pin diameter  $D_f = 38\text{--}559 \text{ }\mu\text{m}$ , pin spacing  $S = 74\text{--}800 \text{ }\mu\text{m}$ , and pin height  $H_f = 90\text{--}845 \text{ }\mu\text{m}$ . Subsequently, new empirical correlations based on the consolidated database were formulated to describe the Nusselt number and fanning friction factor in the micro-pin fin arrays. These correlations provide suitable predictions in comparison with those based on extant correlations.

© 2021 Elsevier Ltd. All rights reserved.

## 1. Introduction

The number of datacenters worldwide has increased substantially over the past two decades to handle the large amount of information and data available. This has led to a corresponding increase in annual electricity consumption. Recent energy statistics indicate that the electricity consumption of a datacenter in the

United States is expected to exceed approximately 73 billion kWh in 2020, and the energy demand for datacenters is expected to further accelerate owing to the emergence of new technologies, such as machine learning, blockchain, 5G, and virtual reality, and video streaming and cloud gaming services [1–3].

In a standard datacenter, approximately half of the overall electricity consumed is used for cooling and supplying power [4,5]. The primary components that require cooling are transistors—for which the integration technology is approaching its limits [6], thereby transitioning towards three-dimensional (3D) integrated circuit (IC) stacked chips in datacenters. Specifically, 3D ICs are stacked vertically to integrate multiple memory types and storage devices, mak-

\* Corresponding author.

E-mail address: [leeh@cau.ac.kr](mailto:leeh@cau.ac.kr) (H. Lee).

URL: <http://atsla.cau.ac.kr> (H. Lee)

**Nomenclature**

$A_h$	heated area
$A_f$	surface area of pin fin
$A_{min}$	minimum transverse area of pin fin array
$C_p$	specific heat
$D_f$	pin fin diameter
$D_w$	transversal diameter of pin fin
$f$	friction factor
$h$	heat transfer coefficient
$H_f$	pin fin height
$I$	current
$k$	thermal conductivity
$N_{tot}$	total number of pin fins
$N_L$	total number of micro-pin fin rows
$m$	fin constant
$\dot{m}$	mass flow rate
$\eta_f$	fin efficiency
$Nu$	Nusselt number
$\Delta P$	pressure drop
$P_f$	cross-section perimeter of pin fin
$Pr$	Prandtl number
$q''$	heat flux
$Q$	volumetric flow rate
$R_{tot}$	total thermal resistance
$Re$	Reynolds number
$S_T$	transverse spacing
$T_b$	micro-pin fin base temperature
$T_f$	fluid temperature
$TPI$	thermal-hydraulic performance index
$u_{in}$	inlet fluid velocity
$u_{max}$	maximum fluid velocity
$V$	voltage

**Greek symbols**

$\varepsilon$	porosity
$\eta_f$	fin efficiency
$\lambda$	pumping power
$\mu$	viscosity
$\rho$	density
$\Phi$	viscosity loss

**Subscripts**

$avg$	average
$b$	base
$CFD$	computational fluid dynamics
$Exp$	experimental
$eff$	effective
$f$	fluid
$h$	heater
$loss$	system losses variable
$min$	minimum
$max$	maximum
$tot$	total

ing it easier to develop heterogeneous computer architectures [7]. In addition, using through-silicon via technology, the length of the wires connecting the chips can be reduced, improving power efficiency [8–10]. However, stacking makes it difficult to dissipate heat using conventional thermal management techniques, resulting in excessive thermal management costs and low cooling efficiency, limiting the commercialization of these high-performance 3D ICs.

Over the past few decades, thermal engineers have attempted to minimize the electrical stability and electrical performance issues in devices caused by overheating resulting from the exponen-

tial increase in the thermal dissipation requirements of ICs [11]. Classical single-side indirect cooling methods to extract heat from the backside of the silicon die using microchannels [12–14], jet impingement [15], and 3D manifold microchannels [16,17] have been proposed. However, their performances are still limited by the high thermal resistance of thermal interface materials. Consequently, several recent studies have focused on embedded cooling, which involves the direct integration of cooling structures between stacked chips [18–22].

Traditional rectangular microchannels have also been applied to cool 3D ICs [23]. However, implementation of this design proved unsuccessful due to high pressure drops caused by narrow gaps between the 3D stacks [24]. The micro-pin fin array exhibits potential for heat transfer while offering a relatively low pressure drop compared to that of traditional microchannels [25]. Kosar and Peles investigated the heat transfer and pressure drop characteristics of micro-pin fins fabricated on silicon structures for cooling electronics in the early 2000s. In a series of studies, they investigated the heat transfer performance and pressure drop for micro-pin fins of various shapes with pin diameters  $D_f = 99.5\text{--}500\text{ }\mu\text{m}$ , pin heights  $H_f = 243\text{--}400\text{ }\mu\text{m}$ , and water and R123 as working fluids [25–30]. Moores and Joshi presented Nusselt number and friction factor correlations for staggered pin fin array using micro-pin fin with  $D_f = 3.67\text{--}3.84\text{ mm}$ ,  $H_f = 2\text{--}4\text{ mm}$ , and water as the working fluid [31]. Prasher *et al.* [32] investigated the thermal and hydraulic performance in staggered micro-pin fin arrays with  $D_f = 55\text{--}153\text{ }\mu\text{m}$  and  $H_f = 155\text{--}310\text{ }\mu\text{m}$  using water as the working fluid. Moreover, they presented possible correlations between the Nusselt number and friction factor. Qu and Siu-ho experimentally investigated single-phase and boiling heat transfer using water as a working fluid in a square staggered pin fin array made of copper with  $D_f = 200\text{ }\mu\text{m}$  and  $H_f = 670\text{ }\mu\text{m}$  [33–37]. Liu *et al.* [38] presented a Nusselt number and friction factor correlation for a staggered pin fin array using a copper-based pin fin with  $D_f = 445\text{--}559\text{ }\mu\text{m}$ ,  $H_f = 3\text{ mm}$ , and water as the working fluid. Experimental demonstrations of temperature distributions for uniform heating [39,40] and nonuniform heating [41,42] in circular and airfoil pin fins using different micro-pin fin geometries have been reported. Water and R245fa were used as working fluids to investigate the heat transfer and pressure drop characteristics of the pin fin with  $D_f = 30\text{--}150\text{ }\mu\text{m}$  and  $H_f = 150\text{--}200\text{ }\mu\text{m}$ . Izci *et al.* [43] studied the thermal and hydraulic performances with various shapes using water as the working fluid. They experimentally measured the Nusselt number and pressure drop across seven different micro-pin fin geometries. Rasouli *et al.* [44] reported the heat transfer and pressure drop characteristics with  $D_f = 257\text{--}573\text{ }\mu\text{m}$  and  $H_f = 193\text{--}1250\text{ }\mu\text{m}$  and a diamond fin shape using PF5060 as the working fluid.

While significant efforts have been made to comprehend the thermal and hydraulic performances of micro-pin fin heat sinks, the effect of geometrical and operational variations on their energy efficiencies in thermal management (due to high fabrication costs and experimental difficulties) have not been investigated. Moreover, most studies utilizing micro-pin fins used water as the working fluid owing to its wide availability and superior thermophysical properties; however, water is not suitable in embedded cooling solutions due to its high electrical conductivity (refer Appendix A in Supplementary Material for a summary of relevant studies).

In this study, the thermal and hydraulic performances in different micro-pin fin heat sinks using various working fluids and geometrical and operating conditions were experimentally and computationally examined. The experimental results were compared with a consolidated database developed based on previous studies; the database consisted of heat transfer and pressure drop data obtained using various working fluids and a wide range of operating conditions and geometries. The cooling efficiency of each of the data points in the consolidated database was compared us-

ing the thermal-hydraulic performance index to provide energy-efficient micro-pin fin heat sink designs and operating conditions. Additionally, a new predictive tool for the Nusselt number and faning friction factor in micro-pin fin arrays based on the consolidated database was developed. The results obtained with the regression model can provide a holistic view for energy management in thermal management systems.

## 2. Experimental methods

### 2.1. Experimental apparatus

#### 2.1.1. Microfabrication process of micro-pin fin array

The micro-pin fin arrays were fabricated on an eight-inch silicon wafer. Fig. 1 shows the detailed fabrication steps. First, a staggered micro-pin fin array, with two pressure ports for pressure measurement, and an inlet orifice on the silicon wafer using a deep reactive ion etching process were fabricated. Then, a silicon dioxide ( $\text{SiO}_2$ ) layer with a thickness of 500 nm was developed on the opposite side of the silicon substrate and coated with a titanium/gold (10/200 nm) thin-film resistive heater. The top side of the micro-pin fin array was covered with a Pyrex plate to enclose the fluid channel while providing an optical view for flow visualization during the experiments. The Pyrex cover and silicon wafer were anodically bonded by sequentially applying voltages of 200 and 600 V at a temperature of 400 °C. Altogether, four different geometric combinations were designed on an eight-inch silicon wafer. Figs. 2(a) and (b–d) show a photograph and scanning electron microscopy (S-3400N Hitachi, Japan) images of the fabricated micro-pin fin sample, respectively.

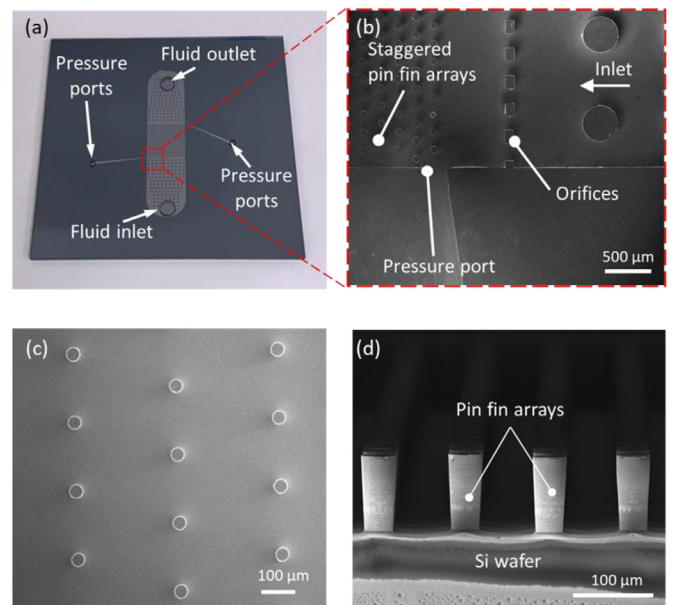


Fig. 2. (a) Test sample after the microfabrication process, (b, c) top-view, and (d) side-view scanning electron microscopy images of micro-pin fin array.

#### 2.1.2. Test module and flow loop facility

Figs. 3(a) and (b) demonstrate the test module assembly and cross-sectional view of the test module, respectively. The microfabricated test sample was installed on the test module, which consisted of polycarbonate (Lexan) and polyether ether ketone (PEEK) slabs for easy connection of the fittings and electrical wiring, while providing sufficient compression strength to avoid bursting during high-pressure tests. Two 1/4" Swagelok fittings served as fluid inlet and fluid outlet, and two 1/16" and two 1/8" fittings served as temperature and pressure measurement ports, respectively.

Fig. 4 shows a schematic of the experimental flow loop used for thermal and hydraulic measurements. The working fluid was circulated using a magnetically driven gear pump (Micropump GA-T23) after passing through a 50- $\mu\text{m}$  filter (FT-4N). The volumetric flow rate was measured at the pump outlet using a flow meter (KIF510). The temperature of the working fluid was adjusted using an electrically powered pre-heater (TECHNE TE-10D) before introducing the fluid into the test module. The surface temperature of the film heater was measured using a thermal-infrared camera (FLIR E75) with a resolution of  $320 \times 240$  pixels. A black spray paint (ELE EP-10) was applied to the surface of the thin-film heater, and the surface emissivity was calibrated before the temperature measurement. The heated fluid was cooled to the ambient temperature using a plate heat exchanger connected to a liquid circulation chiller (Jeitech HH20). The temperature changes of the test module were measured using two K-type thermocouples located in the inlet and outlet plenums. The pressure drop was measured using an absolute pressure transducer (TRAFAG EPI8287) at the inlet and a differential pressure transducer (Omega PX409) connected to the inlet and outlet of the micro-pin fin array.

#### 2.1.3. Test procedure, operating conditions, and uncertainty

Power was supplied to the thin-film resistive heater using a DC power supply (Keysight 6030A). The supplied power was measured with a voltage divider circuit consisting of two resistors with resistances of  $47 \text{ k}\Omega \pm 0.1\%$  and  $3 \text{ k}\Omega \pm 0.1\%$  and a  $0.05 \text{ }\Omega \pm 0.5\%$  shunt resistor. The experiments were conducted by setting the desired fluid flow rate on the pump. The heater power was supplied in the thin-film heater. The heated surface temperature and fluid temperatures and pressures at the inlet and outlet of the

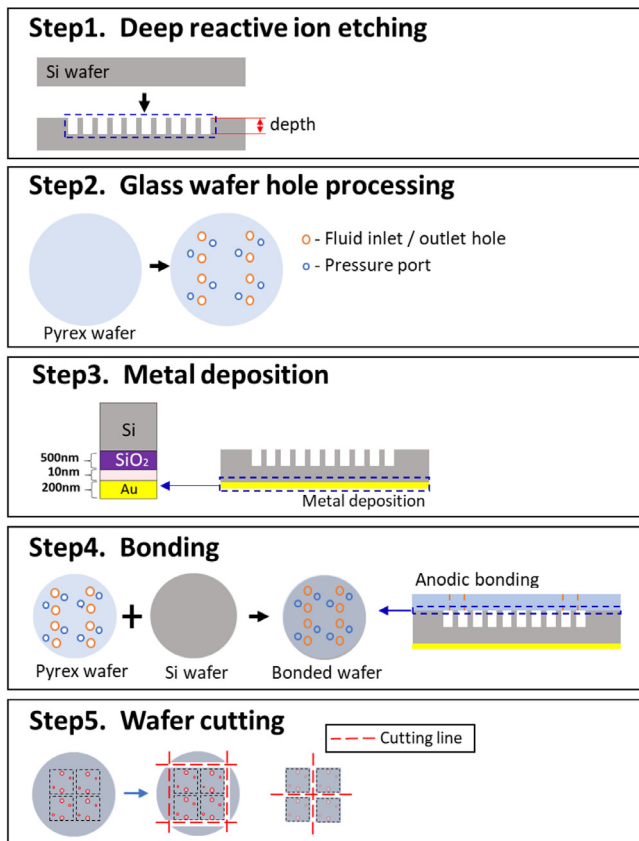


Fig. 1. Overall microfabrication process of embedded micro-pin fin arrays.

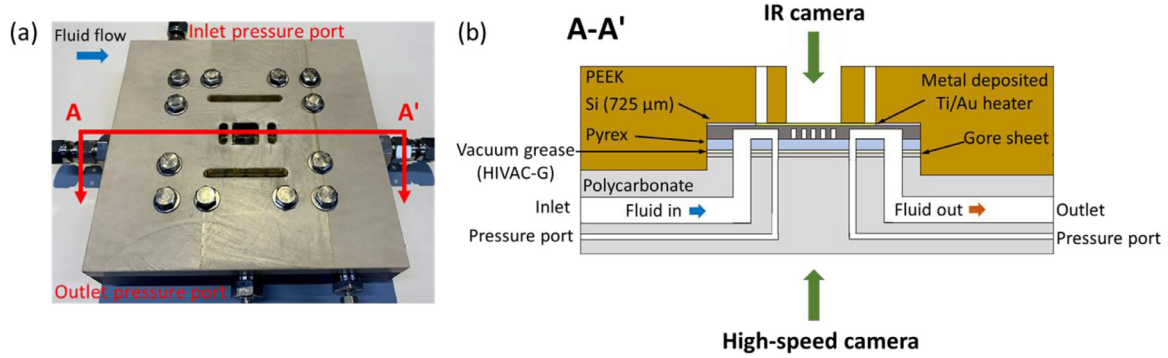


Fig. 3. (a) Photograph of the assembled test module; (b) Schematic of the cross-section of the test module.

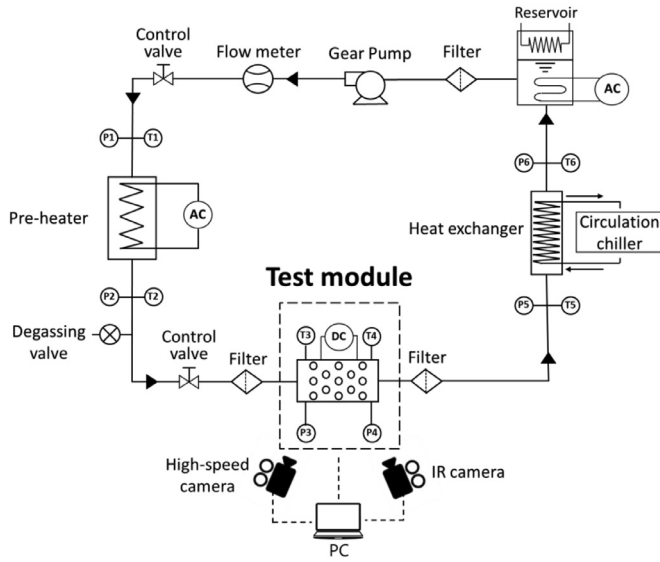


Fig. 4. Schematic of the experimental flow loop.

test module were monitored until the steady state was reached. Once the steady state was reached ( $< \pm 0.3$  °C for 5 min), temperature and pressure measurements were performed for 60 s. Then, the heater input power and flow rate were increased at 20 W/cm<sup>2</sup> and 10 mL/min intervals, respectively, and the procedure was repeated.

NI Compact DAQ and LabVIEW were used to record the flow rate, fluid temperatures and pressures, and input power to the heater. The heated surface temperature was recorded using an IR camera with an accuracy of  $\pm 2\%$ . Uncertainties for the measurements were calculated using a method proposed by Taylor and Kuyatt [45]. K-type thermocouples with an accuracy of  $\pm 0.4\%$  were used to measure the temperatures. The pressure drop along the micro-pin fin array was measured with a differential pressure transducer (Omega PX409) and an absolute pressure transducer (Trafag EPI-8287), both with accuracies of  $\pm 0.5\%$ . The DC power supply for the heater had an accuracy of  $\pm 0.3$  W. Consequently, the heat transfer coefficient (*HTC*) and pressure drop had mean uncertainties of 7.1% and 8.6%, respectively.

The operating conditions were as follows: fluid inlet pressure  $P_{in}$  of 161.6–227.7 kPa; fluid inlet temperature  $T_{in}$  of 21.5–25.2 °C; volumetric flow rate  $Q$  of 41.2–82.4 mL/min; heat flux  $q''$  of 0–55.4 W/cm<sup>2</sup>. Table 1 summarizes the operating conditions of the experiment and geometrical parameters of the micro-pin fin.

## 2.2. Computational modeling

Computational simulations were performed using ANSYS FLUENT 19.2 to validate the experimental results. The constitutive equations are as follows: continuity equation

$$\nabla \cdot u = 0, \quad (1)$$

conservation of momentum

$$\rho(u \cdot \nabla u) = -\nabla P + \mu \nabla^2 u + \rho g, \quad (2)$$

conservation of energy

$$\rho C_p(u \cdot \nabla T) = \nabla(k \nabla T) + \mu \Phi, \quad (3)$$

where  $u$  is the velocity vector,  $\rho$  is the density,  $P$  is the static pressure,  $\mu$  is the dynamic viscosity, and  $k$  is the thermal conductivity of the working fluid;  $g$  is the acceleration due to gravity,  $\Phi$  is the viscosity loss,  $C_p$  is the specific heat, and  $T$  is the temperature. Single-phase steady state simulations were conducted using the mass-flow inlet and pressure-outlet boundary conditions. The pressure and velocity were coupled using semi-implicit method for pressure-linked equations (SIMPLE) algorithm, and the gradient was discretized using least squares cell-based method. Pressure discretization was set to second-order, while second-order upwind was used for momentum and energy discretization. The effects of turbulence due to the micro-pin fins were considered using the shear stress transport  $k-\omega$  turbulence model. The convergence criteria of the solutions were set to a residual of less than  $10^{-6}$  for continuity, velocities,  $k$ , and  $\omega$  along with a residual of less than  $10^{-12}$  for energy. An adiabatic boundary condition was set on the top surface of the Pyrex cover, while a constant heat flux was set on the heated bottom surface.

Fig. 5 shows a schematic of the computational domain with appropriate boundary conditions. Temperature-dependent properties were adopted for the fluid and solids. Mesh independence was verified using over 7.9 million hexahedral elements, and a case of 4.9 million cells was finally adopted for the results. The detailed results of the mesh dependency test are provided in Table 2.

In addition to simulating the two geometrical structures used in the experiment, we numerically evaluated three additional micro-pin fin configurations with various pin fin spacings to investigate their effect on both heat transfer and pressure drop in micro-pin fin heat sinks. The added geometries are as follows: (1)  $S_T = 100$   $\mu$ m,  $S_L = 300$   $\mu$ m, (2)  $S_T = 300$   $\mu$ m,  $S_L = 200$   $\mu$ m, (3)  $S_T = 300$   $\mu$ m,  $S_L = 100$   $\mu$ m; they all have the same fin diameter and height as the structures used in the experiment. The operating conditions were analyzed by setting five flow rates ( $Q = 40$ –80 mL/min) and three heat fluxes ( $q'' = 17$ –55 W/cm<sup>2</sup>). A total of 36 cases were analyzed.



**Table 1**  
Operating conditions and micro-pin fin geometrical parameters.

Case	$D_f$ [μm]	$H_f$ [μm]	$S_L$ [μm]	$S_T$ [μm]	Arrangement	Shape	$N_{Row}$	$N_{Column}$	$T_{in}$ [°C]	$P_{in}$ [kPa]	$Q$ [mL/min]	$q''$ [W/cm <sup>2</sup> ]
1	38.1	90.9	301	301	Staggered	Circular	34	34	21.5 – 23.5	164.7 – 208.9	41.2 – 81.1	17.1 – 54.4
2	38.1	90.9	302	198	Staggered	Circular	50	34	24.2 – 25.2	161.6 – 227.7	41.9 – 82.4	17.7 – 55.4

**Table 2**  
Mesh independency test results.

Number of elements	$\Delta P$ [kPa]	Outlet temperature [K]	Average heater temperature [K]
1,464,008	29.6	321.1	366.9
2,493,866	28.3	321.2	368.1
3,161,592	27.5	321.9	371.0
4,938,930	27.7	322.1	372.0
7,944,248	27.5	322.1	371.4

### 2.3. Data reduction

The effective heat flux  $q''_{eff}$  of the heater to the micro-pin fin array is determined by subtracting heat loss to the surroundings from the power input to the thin-film heater as follows:

$$q''_{eff} = q'' - q''_{loss}, \quad (5)$$

$$q'' = V \cdot I / A_h, \quad (6)$$

where  $q''$  is the total power input to the thin-film heater, and  $q''_{loss}$  is the heat loss to the ambient. As represented in Eq. (6), where  $V$  is the voltage supplied to the heater and  $I$  is the current,  $q''$  can be determined from dividing the power input to the heater by the heated area  $A_h$ . The heat loss to the ambient was determined by the energy balance between the heater input power and the sensible heat increase of the fluid during the single-phase heat transfer experiment. The average heat transfer coefficient is determined as follows:

$$h = \frac{q''_{eff} A_h}{\left[ (A_h - N_{tot} \frac{\pi D_f^2}{4}) + (\pi D_f H_f N_{tot} \eta_f) \right] (T_b - T_f)} \quad (7)$$

Here,  $D_f$  and  $H_f$  are the pin fin diameter and pin fin height, respectively;  $T_b$  is the average temperature at the base of the flow pin fin array, which was estimated using the one-dimensional

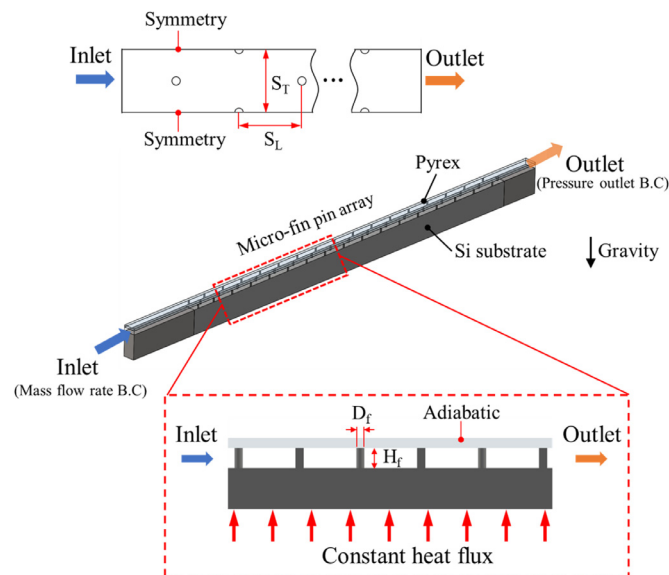


**Fig. 5.** Computational domain of a unit cell of the micro-pin fin channels.

heat conduction from the thin-film heater through the silicon substrate considering the temperature-dependent thermal conductivity of silicon;  $T_f$  is the bulk fluid temperature along the micro-pin fin array;  $N_{tot}$  is the total number of pin fins;  $\eta_f$  is the fin efficiency, which can be determined by

$$\eta_f = \frac{\tanh(mH_f)}{mH_f} \quad (8)$$

where  $m$  is the fin constant defined as

$$m = \sqrt{\frac{hP_f}{k_s A_f}} \quad (9)$$

In Eq. (9),  $h$  is the convective heat transfer coefficient,  $k_s$  is the thermal conductivity of the silicon structure, and  $P_f$  and  $A_f$  are the perimeter and cross-sectional area of the fin, respectively. The average heat transfer coefficient was calculated by solving Eqs. (7)–(9) with the fzero function in MATLAB. Therefore, using the average heat transfer coefficient of the fluid in the micro-pin fin array, the Nusselt number  $Nu$  can be determined as follows:

$$Nu = \frac{hD_f}{k_f}. \quad (10)$$

The experimentally determined fanning friction factor is defined as

$$f = \frac{\Delta P}{2\rho u_{max}^2 N_L} \quad (11)$$

In Eq. (11),  $\Delta P$  is the pressure drop along the micro-pin fin array,  $N_L$  is the number of pin fins in the longitudinal direction of the fluid flow, and  $u_{max}$  is the maximum fluid velocity, which can be determined as follows with the equations below.

$$\text{Inline: } u_{max} = \frac{S_T}{S_T - D_f} u_{in} \quad (12a)$$

$$\text{Staggered: } u_{max} = \max \left( \frac{S_T}{S_T - D_f} u_{in}, \frac{S_T}{2(S_D - D_f)} u_{in} \right). \quad (12b)$$

In the above equations,  $u_{in}$  is the inlet fluid velocity of the channel.

The thermal and hydraulic performances of the micro-pin fin heat sink were compared using the thermal-hydraulic performance index (TPI). The TPI, which was proposed by Gee and Webb, represents the heat transfer performance per unit pressure drop to consider both thermal and hydrodynamic performances. [46] It has been widely used as a measure to compare performances in studies on pin fin configuration [47–50]. It can be calculated as follows:

$$TPI = \frac{(Nu/Nu_o)}{(f/f_o)^{1/3}}, \quad (13)$$

where  $Nu_o$  and  $f_o$  are the reference Nusselt number and fanning friction factor, respectively. Here,  $Nu_o = 5.385$  is used from the fully developed laminar flow in the microchannel, while  $f_o$  is determined under the same conditions using the following relation [51,52]:

$$f_o = \frac{1}{Re} \cdot \left[ 24 + \frac{0.674 Re \cdot D_h}{4L} \right]. \quad (14)$$

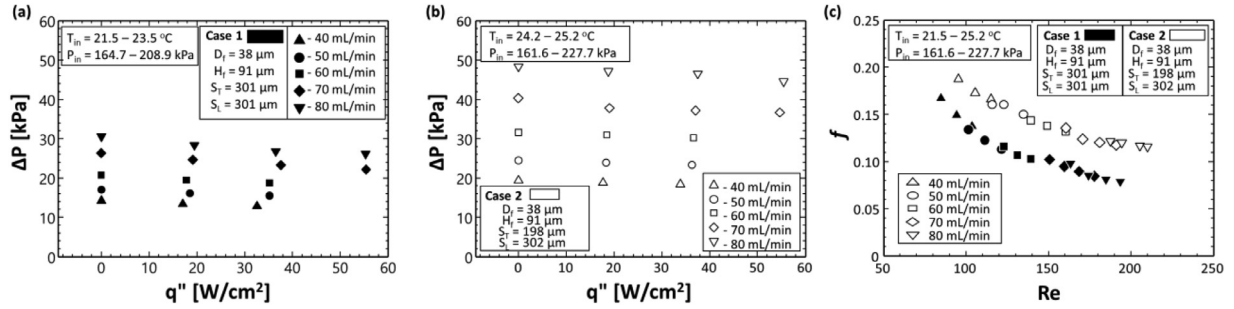


**Fig. 6.** Pressure drop results with different geometries: (a) and (b) pressure drop versus heat flux in Cases 1 and 2, respectively; (c) friction factor as a function of the Reynolds number.

The Reynolds number  $Re$  is calculated based on the hydraulic diameter of the micro-pin fin as

$$Re = \frac{\dot{m} D_f}{\mu A_{min}}, \quad (15)$$

where  $\dot{m}$  is the mass flow rate, and  $\mu$  is the dynamic viscosity of the fluid.

### 3. Results and discussion

#### 3.1. Pressure drop and friction factor

Adiabatic and single-phase hydraulic experiments were conducted to evaluate the pressure drop and friction factor in the micro-pin fin array. The fanning friction factor was calculated using Eq. (11) for the measured pressure drop data using a dielectric 3M Fluorinert FC-72 as the working fluid. Fig. 6 (a) and (b) demonstrate the pressure drop in the micro-pin fin array according to the flow rate and heat flux. Two different geometries (Case 1:  $D_f = 38.1 \mu\text{m}$ ,  $H_f = 90.9 \mu\text{m}$ ,  $S_L = 301 \mu\text{m}$ , and  $S_T = 301 \mu\text{m}$ ; Case 2:  $D_f = 38.1 \mu\text{m}$ ,  $H_f = 90.9 \mu\text{m}$ ,  $S_L = 302 \mu\text{m}$ , and  $S_T = 198 \mu\text{m}$ ) were compared at volumetric flow rate  $Q$  and heat flux  $q''$  ranges of 41.2–82.4 mL/min and 0–55.4 W/cm², respectively.

From Fig. 6, it can be observed that the pressure drop increases with the flow rate, and Case 2 shows a higher pressure drop than Case 1 owing to the geometric effect under all flow rate conditions. The pressure drop in Case 1 is 12.8–30.5 kPa, while that in Case 2 is approximately 40% higher (18.4–48.3 kPa) owing to the smaller pin spacing. For both samples, the pressure drop slightly decreases as the heat flux increases because the dynamic viscosity of the fluid decreases with increasing fluid temperature under the same flow rate. Fig. 6(c) shows the friction factor  $f$  as a function of  $Re$ . In Case 1, the range of  $f$  is 0.08–0.17 with  $Re = 84.4$ –193.1, and in Case 2, the range of  $f$  is 0.12–0.19 with  $Re = 95.4$ –210. Be-

cause of the geometrical effect with different spacing between the pin fins, Case 2 with a high pressure drop under similar operating condition has a relatively high  $f$  of 34.1% than Case 1. In the same flow range, the  $f$  is slightly decreased with the heat flux owing to the lower viscosity as the fluid temperature increases. Furthermore,  $f$  decreases as  $Re$  increases in all cases. In the small- $Re$  range ( $Re < 100$ ),  $f$  decreases sharply owing to the laminar flow. As  $Re$  increases because of the increased flow rate,  $f$  decreases relatively slowly owing to the vortex generated behind the micro-pin fin and the increased pressure drop.

#### 3.2. Computational modeling results

Computational modeling was used to validate the thermal and hydraulic performances determined from the experiments, suggest possible improvements, and determine the optimal design. Fig. 7 compares the experimentally obtained pressure drop and averaged heater and fluid temperatures with those obtained from the simulations. The maximum errors of the total pressure drop and heater temperature obtained were 3.6% and 1.3%, respectively, which are within the measurement accuracy range of the pressure transducer used in the experiment. Fig. 8 compares the analytical and experimental values of  $f$  and  $Nu$  considering the MAE. The computational results were consistent with the experimental data. In Cases 1 and 2, the MAE of  $f$  was 4.6% and 3.6%, respectively, that of  $Nu$  was 3.2% and 3.8%, respectively, and the overall MAE was 3.5%.

Fig. 9 shows the computational results obtained from all five micro-pin fin configurations: two experimental geometries and three additional configurations having various pin fin spacings. Fig. 9(a) shows the  $TPI$  according to the  $Re$ . This figure clearly indicates that a smaller longitudinal spacing ( $S_L$ ), such as in the case of  $S_T = 300 \mu\text{m}$  and  $S_L = 100 \mu\text{m}$  and  $S_T = 300 \mu\text{m}$  and  $S_L = 200 \mu\text{m}$ , provides a relatively higher  $TPI$  compared to the case of  $S_T = 300$

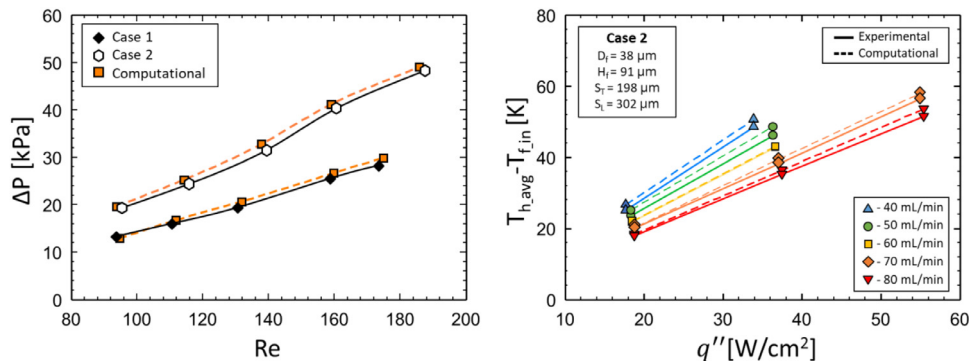


**Fig. 7.** Experimental and simulated (a) pressure drop as a function of the Reynolds number and (b) average heater temperature and fluid inlet temperature as a function of the heat flux.

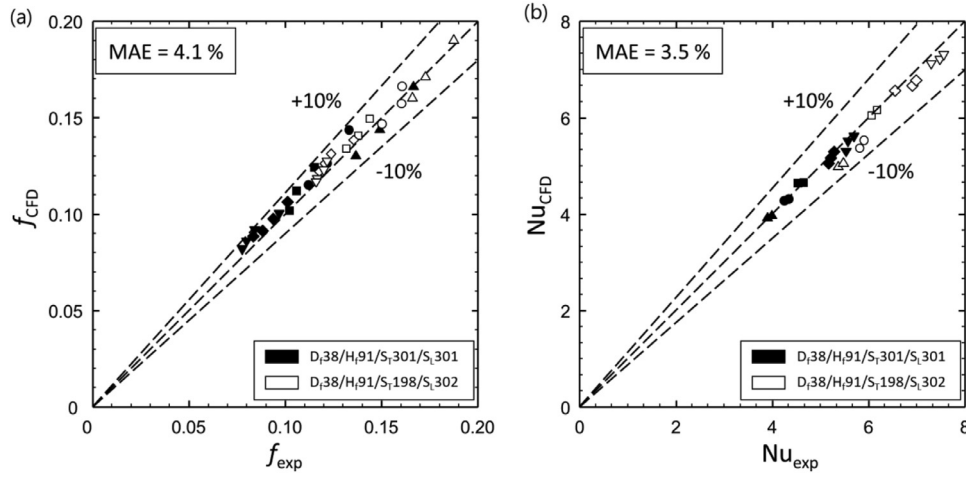


Fig. 8. Simulated and experimental (a) friction factor and (b) Nusselt number.

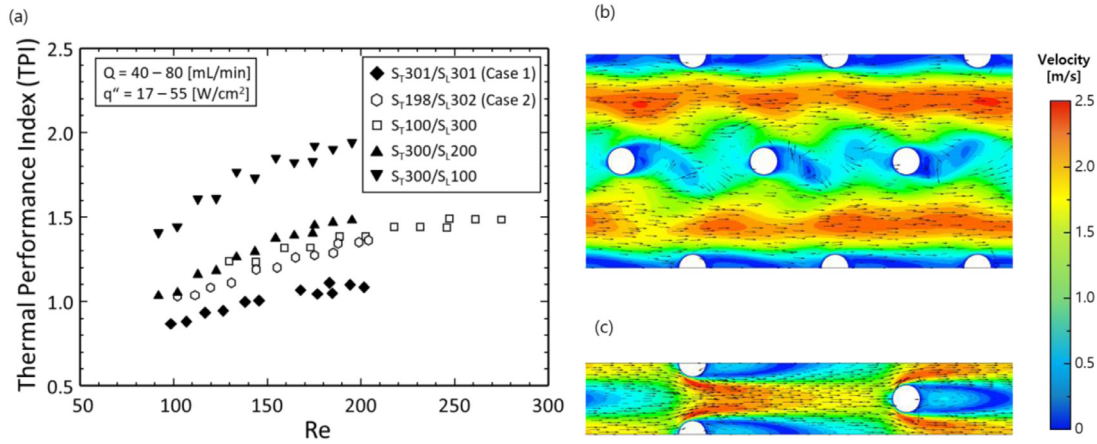


Fig. 9. (a) Simulated thermal performance index as a function of Reynolds number, (b) velocity contour of  $S_T = 300 \mu\text{m}$ ,  $S_L = 100 \mu\text{m}$  and (c)  $S_T = 100 \mu\text{m}$ ,  $S_L = 300 \mu\text{m}$ .

$\mu\text{m}$  and  $S_L = 300 \mu\text{m}$  within the ranges of  $Q = 40\text{--}80 \text{ mL/min}$  and  $q'' = 17\text{--}55 \text{ W/cm}^2$ . It is also evident that a smaller transversal spacing ( $S_T$ ) leads to a higher TPI. Fig. 9(b) and (c) show the velocity contour and normalized vector with the selected two cases of  $S_T = 300 \mu\text{m}$ ,  $S_L = 100 \mu\text{m}$  and  $S_T = 100 \mu\text{m}$ ,  $S_L = 300 \mu\text{m}$  at a mass flow rate of  $60 \text{ mL/min}$  and heat flux of  $36 \text{ W/cm}^2$ . As shown in Fig. 9(b) and (c), the wake flow behind the pin appears remarkably for  $S_T = 300 \mu\text{m}$ ,  $S_L = 100 \mu\text{m}$ , and corresponds to an improvement in the thermal performance. In contrast, a lower wake flow is observed for a smaller  $S_T$ , which result in a relatively lower amount of heat transfer.

### 3.3. Heat transfer performance

The Nusselt number  $Nu$  and total thermal resistance  $R_{tot}$  were determined to investigate the thermal performance of the micro-pin fin heat sinks. Fig. 10 shows the temperature distributions of the heated surface from the selected case, which were obtained from the IR thermal images. The fluid temperature increases as the fluid flows from the left to the right. It appears that the highest temperature is in the direction skewed to the right, and not the far right because heat spreads to the substrate at the edges. In the range of  $q'' = 40\text{--}100 \text{ W/cm}^2$ , as the heat flux value increases by  $20 \text{ W/cm}^2$ , the temperature steadily increases as expected. The deviation in temperature increases as the heat flux increases. Fig. 11 shows the area-averaged  $Nu$  obtained by Eq. (10). The figure illus-

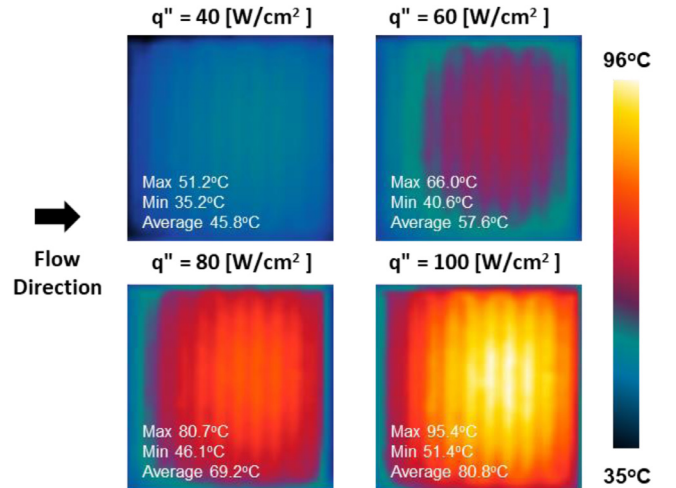


Fig. 10. IR images of temperature distributions on heater surface with increase in power input by  $20 \text{ W/cm}^2$ , operating at a fixed mass flow rate of  $120 \text{ g/min}$ .

trates that in Cases 1 and 2,  $Nu$  varies between 3.90 and 5.69 and between 5.36 and 7.56, respectively. At the same flow rate,  $Nu$  is up to 37.5% higher in Case 2 compared to Case 1 because the denser fin spacing increases the higher maximum fluid velocity  $u_{max}$  and

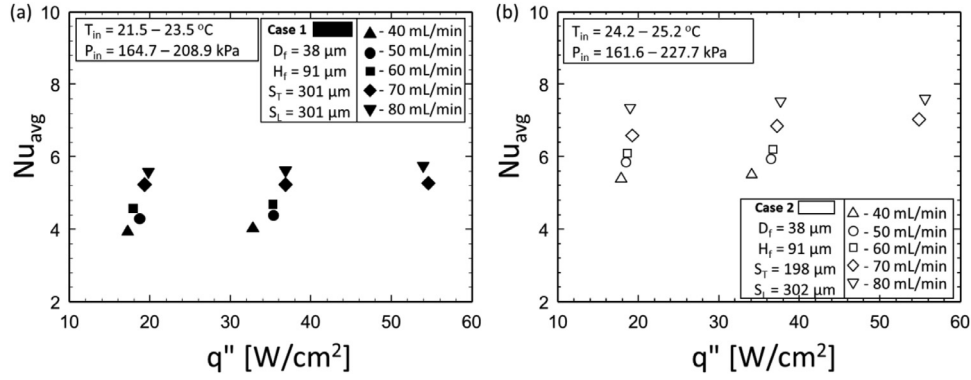


Fig. 11. Average Nusselt number as a function of the heat flux in micro-pin fin arrays for (a) Case 1 and (b) Case 2.

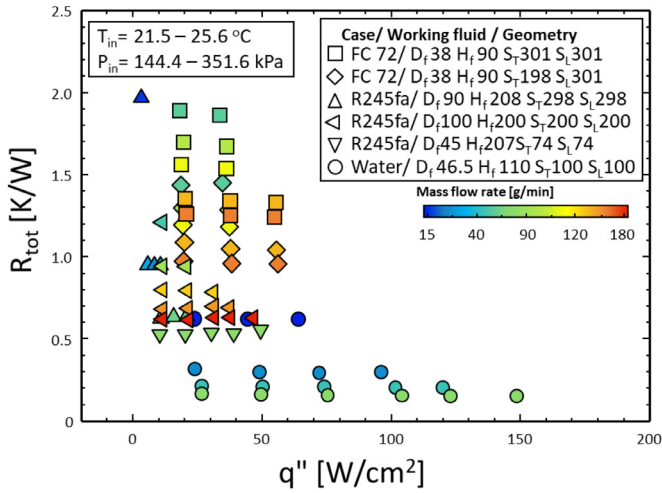


Fig. 12. Experimentally determined thermal resistance at different heat fluxes.

$Re$ ,  $Nu$  increases slightly with increasing heat flux at the same flow rate because the higher fluid temperature results in lower fluid viscosity.

Fig. 12 shows a plot of  $R_{tot}$  as a function of the heat flux and flow rate obtained under different experimental conditions [53,54]. Here,  $R_{tot}$  is the sum of the conduction thermal resistance  $R_{cond}$  through the silicon substrate, convection thermal resistance  $R_{conv}$  between the channel base and fluid, and advection thermal resistance  $R_{adv}$  caused by the increase in the sensible heat of the fluid along the channel. Mathematically,  $R_{tot}$  can be expressed as follows:

$$R_{tot} = R_{cond} + R_{conv} + R_{adv} = \frac{T_h - T_{f,in}}{q''_{eff} A_h}, \quad (16)$$

where

$$R_{cond} = \frac{t_{si}}{k_s A_h}, \quad (17a)$$

$$R_{conv} = \frac{1}{h A_h}, \quad (17b)$$

$$R_{adv} = \frac{T_f - T_{f,in}}{q''_{eff} A_h}. \quad (17c)$$

In the equations above,  $T_h$  is the surface temperature of the heater, and  $t_{si}$  is the thickness of the silicon substrate. As can be seen in Fig. 12,  $R_{tot}$  decreases with increasing flow rate in most

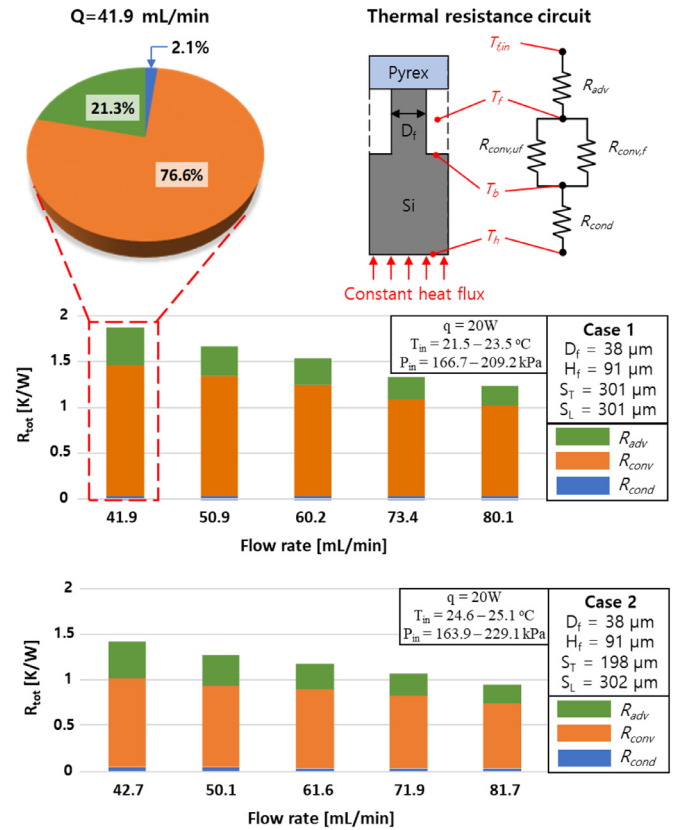
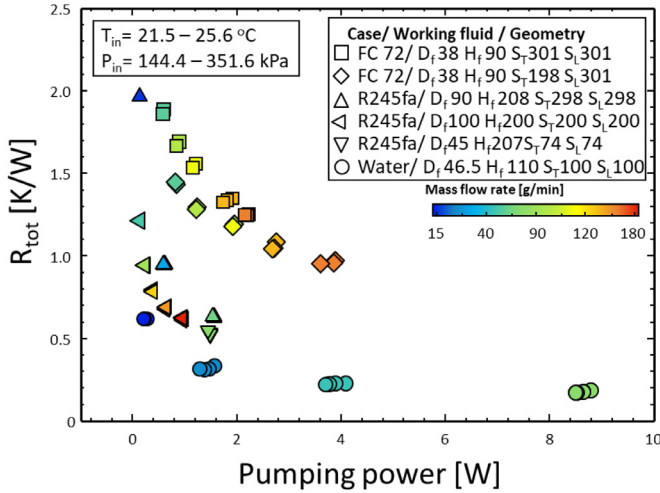


Fig. 13. Total thermal resistance and portions of different thermal resistance components.

cases; this is because of the increasing  $HTC$ . For the same working fluid, a smaller spacing leads to lower  $R_{tot}$  owing to the higher convective heat transfer from denser pin fins. As expected,  $R_{tot}$  decreases with increasing flow rate but remains approximately constant with the applied heat flux because of the characteristics of single-phase convective heat transfer. Lower  $R_{tot}$  are obtained with denser pin fins (Cases 2, 4, and 5) than with relatively sparsely packed pin fins (Cases 1 and 3). It can be inferred that  $R_{cond}$  and  $R_{adv}$  are similar under similar operating conditions; however, relatively large changes are observed in  $R_{conv}$  with different geometries and operating conditions.

Fig. 13 depicts the portions of each thermal resistance component. The two samples show a similar thermal resistance trend, and  $R_{cond}$  and  $R_{adv}$  have relatively small variations. However,  $R_{conv}$





**Fig. 14.** Experimentally determined thermal resistance as a function of the required pumping power.

depends on the geometry and contributes majorly to  $R_{tot}$  (68.6–81.2%). The portion of  $R_{cond}$  is 1.9–3.7%, which is the smallest, and  $R_{adv}$  has a contribution of 16.9–27.7% and decreases as the flow rate increases owing to the decreasing difference between  $T_f$  and  $T_{f,in}$ .

### 3.4. Thermal–hydraulic performance of micro-pin fin

The heat transfer performance is vital for cooling; however, the hydraulic performance should be considered simultaneously for the energy efficiency of thermal management because it determines the power consumption of the cooling system. The required cooling energy is related to the pumping power  $\mathcal{A}$ , which is determined from the pressure drop along the micro-pin fin array and desired flow rate  $Q$  as follows:

$$\mathcal{A} = \Delta P \cdot Q. \quad (18)$$

In conventional internal cooling systems, the heat transfer performance increases with the flow rate, and a higher  $\mathcal{A}$  is required to supply more coolant into the heat sink. Therefore, the thermal resistance and required cooling energy are inversely proportional, and it is necessary to optimize the thermal and hydraulic performances simultaneously. Fig. 14 shows a plot of  $R_{tot}$  as a function of the pumping power required for supplying fluid into the test section for the same data points used in Fig. 12. The figure indicates that higher flow rates result in a large required pumping power. At the given pumping power, denser pin fins (Cases 2, 4, and 5) have smaller  $R_{tot}$  owing to the higher  $HTC$  from the larger effective heat transfer area. However, the difference in  $R_{tot}$  among the three cases decreases as the flow rate increases, while  $\mathcal{A}$  increases rapidly owing to the sharp increase in the pressure drop. Therefore, sparsely packed pin fins are more energy efficient at low  $\mathcal{A}$ , whereas densely packed pin fins are more energy efficient at high  $\mathcal{A}$ . These results indicate that the optimal operating geometric and operating conditions can be determined based on the target  $R_{tot}$  and  $\mathcal{A}$ .

### 3.5. Consolidated micro-pin fin database

The database listed in Table 3 was built using previous experimental studies on micro-pin fin arrays with various geometrical and operational conditions. Using the database, the thermal and hydraulic performances of micro-pin fin arrays were compared with various geometrical and operational conditions to provide guidance for the design of thermal management systems using micro-pin fin heat sinks. The data used for the dataset were

amassed from previous studies performed in our laboratory [53,54] and by other researchers [55–59]. Altogether, 256  $Nu$  and  $f$  data points were collected from seven sources. Water, R245fa, and FC-72 were used as working fluids with 21 geometric combinations. The porosity  $\varepsilon$ , which is defined as  $\varepsilon = V_f / V_{tot}$ , was used to represent the pin fin density.

Fig. 15 shows plots of the experimentally determined  $f$  and  $Nu$  as functions of  $Re$  for the 21 geometries obtained from the dataset. Predictably, high-pressure drops are associated with large  $Re$ , high viscosity of working fluid, low porosity, and square and diamond pin fin shapes. As shown in Fig. 15 (a), at low  $Re$  ( $Re < 100$ ),  $f$  decreases rapidly with increasing  $Re$ , while it decreases slowly at high  $Re$  ( $Re > 100$ ); this can be attributed to the increasing mixing behind the fins, as observed in [54]. At the given  $Re$  ranges, water exhibits a higher pressure drop than other working fluids at similar geometric and operating conditions; this can be attributed to the relatively high viscosity of water compared to that of R245fa and FC-72. A large  $H_f$  and low porosity due to the high  $S_T$ ,  $S_L$ , or  $D_f$  result in a high pressure drop. Under the given operating conditions, square and diamond pin fins exhibit higher pressure drops than circular and ellipse pin fins.

Fig. 15(b) shows a plot of  $Nu$  as a function of  $Re$  with the 21 different micro-pin fin array geometries. The figure shows that  $Nu$  tends to increase with  $Re$ . This is attributed to the decrease in the thermal boundary layer thickness with increasing velocity and the increase in the maximum fluid velocity between the pin fins, which provides active flow mixing and secondary flow in the micro-pin fin array [54,60–62]. At  $Re < 100$ ,  $Nu$  significantly depends on the geometry rather than the operating conditions (a small porosity leads to high  $Nu$ ). However, the operating conditions have a substantial effect on  $Nu$  than the geometry at  $Re > 100$ .

Fig. 16 shows a plot of the  $TPI$  as a function of  $Re$ . This figure enables a clear visualization of the variations in thermal and hydraulic performances with different  $Re$  ranges. A high  $TPI$  corresponds to a relatively high heat transfer performance with a low pressure drop and thus, an energy-efficient thermal design. Although convection cooling using water (Cases 8–21) has a higher  $HTC$  than other refrigerants owing to the superior thermal properties of water [63], it leads to a relatively low  $TPI$  because a high viscosity induces a relatively high pressure drop. R245fa leads to a higher  $TPI$  than water because it induces a lower pressure drop. In addition, the  $TPI$  may vary for the same working fluid depending on the operating conditions and geometries. For example, a small porosity provides a high  $TPI$  in the low  $Re$  region owing to its better thermal performance; however, the large pressure drop exacerbates the increase in  $TPI$  with  $Re$  (Cases 5–7 and Cases 20 and 21). In Case 6 ( $\varepsilon = 0.804$ ), the  $TPI$  at  $Re < 400$  is higher than in Case 5 ( $\varepsilon = 0.931$ ); however, the trend is reversed at  $Re > 400$  owing to the rapid increase in the pressure drop as  $Re$  increases. The elliptical pin fin shape (Cases 14 and 17) exhibits a better thermal performance and lower pressure drop than the square and diamond shapes; with the elliptical pin fin shape, the  $TPI$  increases with  $Re$ . In contrast, the square and diamond shapes lead to a relatively high pressure drop compared to the thermal performance, resulting in a relatively low  $TPI$ .

### 3.6. Proposed correlations

In this section, the potential predictive correlations for the friction factor and Nusselt number based on the constructed dataset to cover a wide range of geometrical and operational variations in the micro-pin fin heat sink are described. Based on Fig. 15, which shows that  $f$  and  $Nu$  depend on the spacing, diameter, height, and operating conditions, the following equation was derived:

$$f_{pred} = f(S_L, S_T, D_W, H, D_f, Re). \quad (19)$$

**Table 3**  
Porosity and working fluid of micro-pin fin array.

Case	Working fluid	Geometry					Arrangement	Shape	Operating conditions	Authors
		$D_f[\mu\text{m}]$	$H_f[\mu\text{m}]$	$S_L[\mu\text{m}]$	$S_T[\mu\text{m}]$	$\epsilon$				
#1	FC-72	38.1	90.9	301	301	0.987	Staggered	Circular	Re = 84.4 – 210.1 $\dot{m}$ = 41.2 – 82.4 mL/min $T_{in}$ = 21.5 – 25.2 °C $P_{in}$ = 161.6 – 227.7 kPa $q''$ = 17.1 – 55.4 W/cm <sup>2</sup>	Present study
#2	FC-72	193	193	388	198	0.981	Staggered	Diamond	Re = 8 – 1189 $q''$ = 0 – 234 W/m <sup>2</sup> Bulk fluid temperature increased 5°C	Rasouli et al. (2018)
#3					783	0.849				
#4	R245fa	200	845	276	552	0.776	Staggered	Circular	Re = 35.5 – 432.1 $\dot{m}$ = 14.7 – 181.6 g/min $T_{in}$ = 22.2–25.3 °C $P_{in}$ = 205.6–351.6 kPa $q''$ = 2.5 – 48.7 W/cm <sup>2</sup>	Kong et al. (2019)
#5		90	208	298	298	0.931				
#6	Water	100	200	200	200	0.804	Staggered	Circular	Re = 22.8 – 135 $\dot{m}$ = 15.1 – 64.1 g/min $T_{in}$ = 24.3 – 25.6 °C $P_{in}$ = 144.4 – 340.1 kPa $q''$ = 24 – 141.4 W/cm <sup>2</sup>	Kharangate et al. (2018)
#7		45	207	74	74	0.671				
#8		46.5	110	100	100	0.831				
#9	Water	100	110	300	400	0.935	Staggered	Circular	Re = 22.8 – 491.3 $\dot{m}$ = 3.5 – 42.3 mL/min $T_{in}$ = 30 °C	Xu et al. (2018)
#10	Water	152	500	1200	300	0.913	Staggered	Circular	Re = 108.6 – 970.2 $\dot{m}$ = 3 – 182.1 mL/min Q = 50 – 150 W	Liu et al. (2015)
#11					300	0.913				
#12						0.889	Inline	Square		
#13						0.889	Staggered	Square		
#14						0.826	Inline	Ellipse		
#15		400			800	0.879	Staggered	Circular		
#16	Water	447				0.846	Staggered	Diamond	Re = 23.2 – 428.5 $\dot{m}$ = 15 – 200 mL/min $T_{in}$ = 50 °C $P_{in}$ = 101 – 273 kPa	Prasher et al. (2006)
#17		559	155			0.819		Ellipse		
#18		55	155	200	200	0.938		Circular		
#19	Water	125	310	303	303	0.859	Staggered	Circular	Re = 13.1 – 198.1 $\dot{m}$ = 18 – 145 mL / min Voltage applied 0.5V increments	Kosar et al. (2007)
#20		100	243	350	150	0.85				
#21				150		0.64				

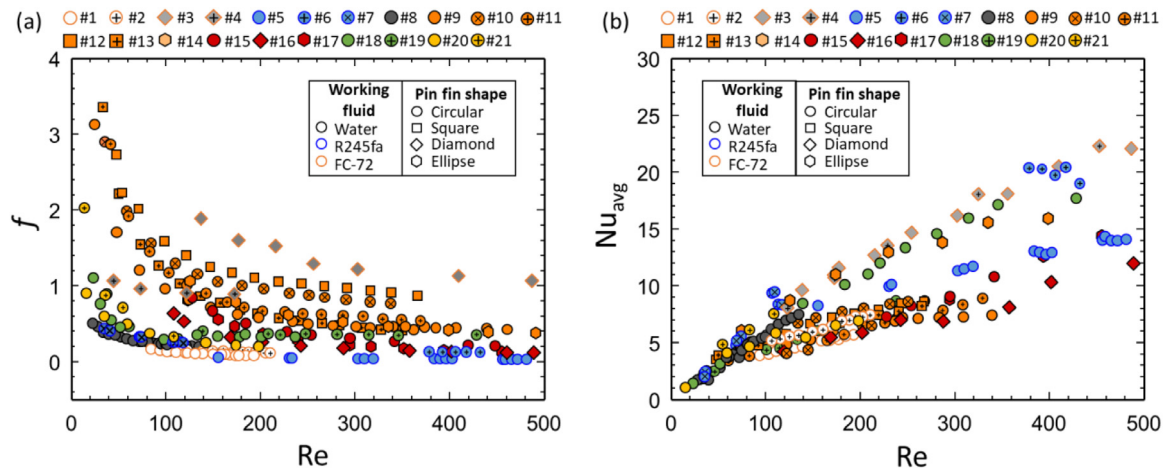


**Fig. 15.** (a) Friction factor and (b) Nusselt number as a function of the Reynolds number for different geometries.

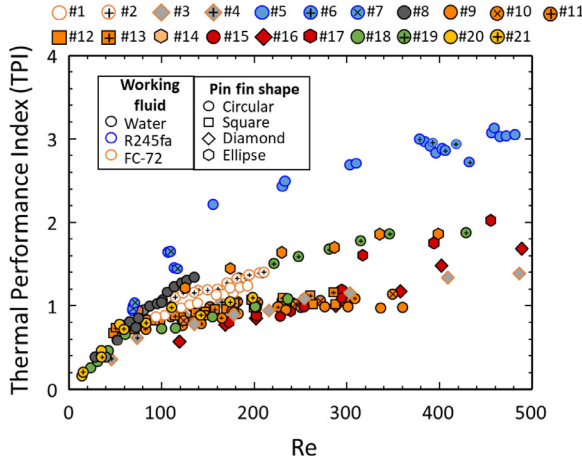


Fig. 16. Thermal performance index as a function of the Reynolds number considering various geometries.

where  $D_w$  is the transversal diameter of the pin fin, which affects the fluid flow. This is considered because different pin fin shapes with the same hydraulic diameter, such as squares and diamonds, result in different pressure drops. To deduce a predictive correlation, a generalized reduced gradient (GRG) nonlinear regression was performed using a descent algorithm, which is known to be effective in deriving correlations for numerous components [64,65]. With the consolidated database, the correlation was predicted through a GRG nonlinear regression analysis, which aims at minimizing the mean absolute error (MAE), as follows:

$$f_{pred} = 8.321 \left( \frac{H_f}{D_f} \right)^{-3.940} \left( \frac{S_L - D_f}{D_f} \right)^{3.596} \left( \frac{S_T - D_f}{D_f} \right)^{-0.203} \left( \frac{D_w}{D_f} \right)^{0.227} Re^{-0.854}, \quad (20)$$

$$Nu_{pred} = 2.380 \left( \frac{H_f}{D_f} \right)^{-1.065} \left( \frac{S_L - D_f}{D_f} \right)^{-0.248} \left( \frac{S_T - D_f}{D_f} \right)^{-0.099} \left( \frac{D_w}{D_f} \right)^{0.167} \frac{1}{3} Pr Re^{0.293}. \quad (21)$$

The MAE was calculated as follows:

$$MAE = \frac{1}{n} \sum_n \frac{|X_{Exp} - X_{Pred}|}{X_{Exp}} \times 100(\%), \quad (22)$$

where  $X_{exp}$  and  $X_{pred}$  are the experimental and predicted data, and  $n$  is the total number of data. Fig. 17 presents comparisons of the predicted and experimental friction factors and Nusselt numbers with the experimentally determined values. The friction factor predicted with the proposed model has a large MAE of 41.7%. However, this MAE is significantly lower than that of the friction factor obtained with existing correlations; it is approximately 20% lower than that of the friction factor predicted by the Kharangate correlation [53], which provides the best prediction among the other correlations proposed in previous studies ( $MAE = 62.9\%$ ). Cases 2, 13, and 15 exhibit optimum results, with MAEs of 5.4%, 3.0%, and 6.6%, respectively; meanwhile, Cases 4, 7, and 21 show the highest MAEs of 100%, 100%, and 99.9%, respectively. The low MAEs of Cases 13 and 15 can be attributed to the ratio of the spacing length to the diameter because their geometric term is close to the median value of the database. In Cases 2, 13, and 15, the  $Re$  range is similar to that observed in the other cases, which indicates that our predicted correlation is appropriate in that range. In Cases 4, 7, and 21, the porosity is significantly lower ( $\varepsilon = 0.64, 0.671$ , and  $0.776$ , respectively) than in the other cases, which may have led to the relatively low accuracy. To achieve better prediction accuracy, a larger number of experimentally determined data points with various operating and geometric conditions is essential. The details of the MAE obtained in each case are presented in **Appendix C of Supplementary Material**.

Similar to the friction factor correlation, the Nusselt number was obtained based on the collected data using the GRG nonlinear regression method. The Nusselt number depends on the Prandtl number  $Pr$ , which is related to the thermal boundary layer thickness of the fluid,  $Re$ , and the geometrical conditions and can be expressed as follows:

$$Nu_{pred} = f(S_L, S_T, D_w, H, D_f, Pr, Re). \quad (23)$$

Fig. 17(b) compares the  $Nu$  derived from the GRG nonlinear regression method in this study with the values obtained from the literature. The  $Nu$  values obtained in adiabatic experimental conditions [56–58], values reported with insufficient information [55] and the point of the temperature of the bottom surface [56,57] were intentionally excluded from this study. As shown in

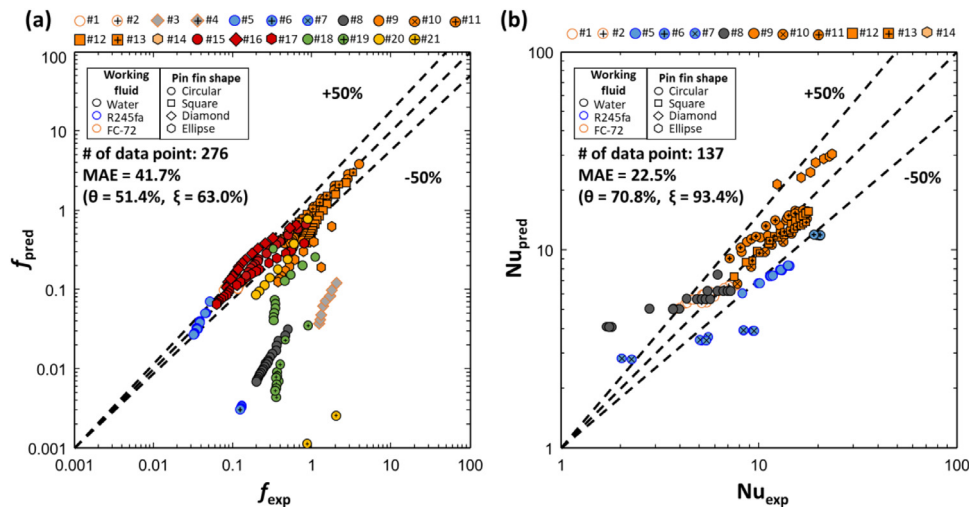


Fig. 17. Comparison of experimental and predicted results of the (a) friction factor and (b) Nusselt number.

Fig. 17(b), the proposed  $Nu$  correlation leads to suitable predictions with  $MAE = 22.5\%$  for the consolidated dataset. The range variation is small compared to that of the friction factor correlation because it was developed with less data. In Cases 1 and 2 (present study) and Cases 9–13 (Xu *et al.* [58]), fairly linear distributions with a slope of approximately 1 are obtained, while the distributions obtained in Cases 5, 7, 8, and 14 have a slope slightly deviating from 1. In Case 5, the experiment was conducted at relatively large  $Re$ , whereas in Cases 7 and 8, the experiment was conducted at relatively small  $Re$ . Notably, the predictions made within a limited  $Re$  range are biased. In Case 14, only an elliptical shape is considered, causing low accuracy. In addition, overprediction of  $Nu$  can be observed in Cases 1 and 2 compared with Case 7 for  $Nu = 5$ –10. This difference can be attributed to the relatively large deviations in the thermo-physical properties of FC-72 compared to those of other working fluids. It appears that the predictions of both  $f$  and  $Nu$  significantly depend on variations in geometries, operating conditions, and the working fluids, which cannot be precisely captured with the current form of the proposed model. Therefore, despite the superiority of the correlations proposed in this paper over previously proposed correlations, further research is required to provide a comprehensive view of the thermal and hydraulic performances in the highly variable conditions of micro-pin fin designs.

#### 4. Conclusions

In this study, the energy-efficient thermal design and management of micro-pin fin heat sinks were investigated. The thermo-hydraulic performance of silicon-based micro-pin fins was analyzed with different geometrical and operating conditions. Experiments were performed with two different geometries (Case 1:  $D_f = 38.1 \mu\text{m}$ ,  $H_f = 90.9 \mu\text{m}$ ,  $S_L = 301 \mu\text{m}$ , and  $S_T = 301 \mu\text{m}$ ; Case 2:  $D_f = 38.1 \mu\text{m}$ ,  $H_f = 90.9 \mu\text{m}$ ,  $S_L = 302 \mu\text{m}$ , and  $S_T = 198 \mu\text{m}$ ) using dielectric fluid FC-72. The pressure drop range  $\Delta P$  was measured to be 12.8–30.5 kPa with  $Re = 84.4$ –193.1 in Case 1 and 18.4–48.3 kPa with  $Re = 95.4$ –210 in Case 2. As the heat flux increased, the pressure drop tended to decrease slightly owing to the decrease in the dynamic viscosity of the fluid. The  $Nu$  range was determined to be 3.90–5.69 in Case 1 and over 37.5% higher (5.36–7.56) in Case 2. At the same flow rate,  $Nu$  increased slightly as the heat flux increased owing to the increase in  $Re$  induced by the increase in the fluid temperature. The total thermal resistance of the micro-pin fin, which comprised three types of resistances, decreased as the flow rate increased and was established primarily in the form of convective thermal resistance. Therefore, in Case 2, where the fin spacings were denser, the thermal resistance was lower than in Case 1 owing to the higher convection heat transfer. The experimental values were verified via CFD simulations. The turbulence model was used to account for the congestion of the flow due to the micro-pin fin array. The maximum error of the pressure drop and heater temperature were 3.6% and 1.3%, respectively, and the  $MAE$  of the experimental and simulation data of  $f$  and  $Nu$  were 4.1% and 3.5%, respectively. For the parametric study of the micro-pin fin, the thermo-hydraulic performance was compared by adding experimental data with similar operating conditions. The  $TPI$  was evaluated as a function of  $Re$  to determine the thermal and hydraulic performances with various parameters. At a low  $Re$ , the thermal performance was low ( $TPI < 1$ ) owing to the weak convective heat transfer effect; however, the  $TPI$  increased as  $Re$  increased. The thermal performance was relatively high with small porosity; however, the  $TPI$  was low owing to the high-pressure drop induced by the increase in  $Re$ . In future research, the thermo-hydraulic performance of micro-pin fin heat sinks should be investigated with a wider range of operating conditions and geometries.

#### Declaration of Competing Interest

None.

#### CRediT authorship contribution statement

**Daewoong Jung:** Data curation, Formal analysis, Investigation, Writing – original draft. **Haeun Lee:** Data curation, Writing – review & editing. **Daeyoung Kong:** Methodology, Data curation. **Eunho Cho:** Formal analysis, Writing – review & editing. **Ki Wook Jung:** Methodology. **Chirag R. Kharangate:** Investigation, Supervision. **Madhusudan Iyengar:** Supervision. **Chris Malone:** Supervision. **Mehdi Asheghi:** Supervision. **Kenneth E. Goodson:** Supervision. **Hyounghoon Lee:** Supervision, Writing – review & editing.

#### Acknowledgments

This work was supported by the National Research Foundation of Korea (NRF) grant funded by the Korea government (MSIT) (No. 2018R1C1B6004468), and the Chung-Ang University Graduate Research Scholarship in 2019. Part of this work was performed at the Stanford Nano Shared Facilities (SNSF), supported by Google, Inc., under Google Faculty Research Award 2017.

The Stanford co-authors would like to acknowledge the U.S. National Science Foundation Engineering Research Center on Power Optimization of Electro-Thermal Systems (POETS) with cooperative agreement EEC-1449548.

#### Supplementary materials

Supplementary material associated with this article can be found, in the online version, at doi:[10.1016/j.ijheatmasstransfer.2021.121192](https://doi.org/10.1016/j.ijheatmasstransfer.2021.121192).

#### References

- [1] A. Shehabi, S. Smith, D. Sartor, R. Brown, M. Herrlin, J. Koomey, E. Masanet, N. Horner, I. Azevedo, W. Lintner, United States Data Center Energy Usage Report (2016), doi:[10.2172/1372902](https://doi.org/10.2172/1372902).
- [2] J.G. Koomey, Growth in data center electricity use 2005 to 2010, A report by Analytical Press, completed at the request of The New York Times 9 (2011) 161 2011.
- [3] Kamiya G. International Energy Agency; 2020. The carbon footprint of streaming video: fact-checking the headlines [internet] <https://www.iea.org/commentaries/the-carbon-footprint-of-streaming-video-fact-checking-the-headlines>
- [4] S.V. Garimella, T. Persoons, J. Weibel, L.-T. Yeh, Technological drivers in data centers and telecom systems: Multiscale thermal, electrical, and energy management, Applied Energy 107 (2013) 66–80, doi:[10.1016/j.apenergy.2013.02.047](https://doi.org/10.1016/j.apenergy.2013.02.047).
- [5] A. Habibi Khalaj, S.K. Halgamuge, A Review on efficient thermal management of air- and liquid-cooled data centers: From chip to the cooling system, Applied Energy 205 (2017) 1165–1188, doi:[10.1016/j.apenergy.2017.08.037](https://doi.org/10.1016/j.apenergy.2017.08.037).
- [6] R.W. Keyes, Fundamental limits of silicon technology, Proceedings of the IEEE 89 (2001) 227–239, doi:[10.1109/5.915372](https://doi.org/10.1109/5.915372).
- [7] S.U. Khan, A.Y. Zomaya, Handbook on data centers, Springer, 2015.
- [8] J.H. Lau, Through-Silicon Vias for 3D Integration, McGraw-Hill, New York, 2013.
- [9] X. Dong, Y. Xie, System-level cost analysis and design exploration for three-dimensional integrated circuits (3D ICs), in: 2009 Asia and South Pacific Design Automation Conference, IEEE, Yokohama, Japan, 2009, pp. 234–241, doi:[10.1109/ASPAC.2009.4796486](https://doi.org/10.1109/ASPAC.2009.4796486).
- [10] J.H. Lau, Overview and Outlook of Three-Dimensional Integrated Circuit Packaging, Three-Dimensional Si Integration, and Three-Dimensional Integrated Circuit Integration, Journal of Electronic Packaging 136 (2014) 040801, doi:[10.1115/1.4028629](https://doi.org/10.1115/1.4028629).
- [11] R. Mahajan, Chia-pin Chiu, G. Chrysler, Cooling a Microprocessor Chip, Proceedings of the IEEE 94 (2006) 1476–1486, doi:[10.1109/JPROC.2006.879800](https://doi.org/10.1109/JPROC.2006.879800).
- [12] C.Y. Zhao, T.J. Lu, Analysis of microchannel heat sinks for electronics cooling, International Journal of Heat and Mass Transfer 45 (2002) 4857–4869, doi:[10.1016/S0017-9310\(02\)00180-1](https://doi.org/10.1016/S0017-9310(02)00180-1).
- [13] J. Lee, I. Mudawar, Two-phase flow in high-heat-flux micro-channel heat sink for refrigeration cooling applications: Part I—pressure drop characteristics, International Journal of Heat and Mass Transfer 48 (2005) 928–940, doi:[10.1016/j.ijheatmasstransfer.2004.09.018](https://doi.org/10.1016/j.ijheatmasstransfer.2004.09.018).



- [14] J. Lee, I. Mudawar, Two-phase flow in high-heat-flux micro-channel heat sink for refrigeration cooling applications: Part II—heat transfer characteristics, *International Journal of Heat and Mass Transfer* 48 (2005) 941–955, doi:[10.1016/j.jheatmasstransfer.2004.09.019](https://doi.org/10.1016/j.jheatmasstransfer.2004.09.019).
- [15] A. Pavlova, M. Amitay, Electronic Cooling Using Synthetic Jet Impingement, *Journal of Heat Transfer* 128 (2006) 897–907, doi:[10.1115/1.2241889](https://doi.org/10.1115/1.2241889).
- [16] J.W. Palko, H. Lee, C. Zhang, T.J. Dusseault, T. Maitra, Y. Won, D.D. Agonafer, J. Moss, F. Houshmand, G. Rong, J.D. Wilbur, D. Rockosi, I. Mykyta, D. Resler, D. Altman, M. Asheghi, J.G. Santiago, K.E. Goodson, Extreme Two-Phase Cooling from Laser-Etched Diamond and Conformal, Template-Fabricated Microporous Copper, *Adv. Funct. Mater.* 27 (2017) 1703265, doi:[10.1002/adfm.201703265](https://doi.org/10.1002/adfm.201703265).
- [17] K.W. Jung, C.R. Kharangate, H. Lee, J. Palko, F. Zhou, M. Asheghi, E.M. Dede, K.E. Goodson, Embedded cooling with 3D manifold for vehicle power electronics application: Single-phase thermal-fluid performance, *International Journal of Heat and Mass Transfer* 130 (2019) 1108–1119, doi:[10.1016/j.jheatmasstransfer.2018.10.108](https://doi.org/10.1016/j.jheatmasstransfer.2018.10.108).
- [18] A. Abdoli, G. Jimenez, G.S. Dulikravich, Thermo-fluid analysis of micro pin-fin array cooling configurations for high heat fluxes with a hot spot, *International Journal of Thermal Sciences* 90 (2015) 290–297, doi:[10.1016/j.jthermalsci.2014.12.021](https://doi.org/10.1016/j.jthermalsci.2014.12.021).
- [19] T.E. Sarvey, Y. Zhang, L. Zheng, P. Thadesar, R. Gutala, C. Cheung, A. Rahman, M.S. Bakir, Embedded cooling technologies for densely integrated electronic systems, in: 2015 IEEE Custom Integrated Circuits Conference (CICC), IEEE, San Jose, CA, USA, 2015, pp. 1–8, doi:[10.1109/CICC.2015.7338365](https://doi.org/10.1109/CICC.2015.7338365).
- [20] C.S. Sharma, M.K. Tiwari, S. Zimmermann, T. Brunschweiler, G. Schlottig, B. Michel, D. Poulikakos, Energy efficient hotspot-targeted embedded liquid cooling of electronics, *Applied Energy* 138 (2015) 414–422, doi:[10.1016/j.apenergy.2014.10.068](https://doi.org/10.1016/j.apenergy.2014.10.068).
- [21] M. Schultz, F. Yang, E. Colgan, R. Polastre, B. Dang, C. Tsang, M. Gaynes, P. Parida, J. Knickerbocker, T. Chainer, Embedded Two-Phase Cooling of Large Three-Dimensional Compatible Chips With Radial Channels, *Journal of Electronic Packaging* 138 (2016), doi:[10.1115/1.4033309](https://doi.org/10.1115/1.4033309).
- [22] D. Lorenzini, C. Green, T.E. Sarvey, X. Zhang, Y. Hu, A.G. Fedorov, M.S. Bakir, Y. Joshi, Embedded single phase microfluidic thermal management for non-uniform heating and hotspots using microgaps with variable pin fin clustering, *International Journal of Heat and Mass Transfer* 103 (2016) 1359–1370, doi:[10.1016/j.jheatmasstransfer.2016.08.040](https://doi.org/10.1016/j.jheatmasstransfer.2016.08.040).
- [23] D. Sekar, C. King, B. Dang, T. Spencer, H. Thacker, P. Joseph, M. Bakir, J. Meindl, A 3D-IC Technology with Integrated Microchannel Cooling, in: 2008 International Interconnect Technology Conference, IEEE, Burlingame, CA, USA, 2008, pp. 13–15, doi:[10.1109/IITC.2008.4546911](https://doi.org/10.1109/IITC.2008.4546911).
- [24] X. Zhang, X. Han, T.E. Sarvey, C.E. Green, P.A. Kottke, A.G. Fedorov, Y. Joshi, M.S. Bakir, Three-Dimensional Integrated Circuit With Embedded Microfluidic Cooling: Technology, Thermal Performance, and Electrical Implications, *Journal of Electronic Packaging* 138 (2016) 010910, doi:[10.1115/1.4032496](https://doi.org/10.1115/1.4032496).
- [25] Y. Peles, A. Koşar, C. Mishra, C.-J. Kuo, B. Schneider, Forced convective heat transfer across a pin fin micro heat sink, *International Journal of Heat and Mass Transfer* 48 (2005) 3615–3627, doi:[10.1016/j.jheatmasstransfer.2005.03.017](https://doi.org/10.1016/j.jheatmasstransfer.2005.03.017).
- [26] A. Koşar, Y. Peles, Boiling heat transfer in a hydrofoil-based micro pin fin heat sink, *International Journal of Heat and Mass Transfer* 50 (2007) 1018–1034, doi:[10.1016/j.jheatmasstransfer.2006.07.032](https://doi.org/10.1016/j.jheatmasstransfer.2006.07.032).
- [27] A. Koşar, Y. Peles, Convective flow of refrigerant (R-123) across a bank of micro pin fins, *International Journal of Heat and Mass Transfer* 49 (2006) 3142–3155, doi:[10.1016/j.jheatmasstransfer.2006.02.013](https://doi.org/10.1016/j.jheatmasstransfer.2006.02.013).
- [28] A. Kosar, Y. Peles, TCPT-2006-096.R2: Micro Scale pin fin Heat Sinks — Parametric Performance Evaluation Study, *IEEE Trans. Comp. Packag. Technol.* 30 (2007) 855–865, doi:[10.1109/TCAPT.2007.906334](https://doi.org/10.1109/TCAPT.2007.906334).
- [29] A. Koşar, Y. Peles, Thermal-Hydraulic Performance of MEMS-based Pin Fin Heat Sink, *Journal of Heat Transfer* 128 (2006) 121, doi:[10.1115/1.2137760](https://doi.org/10.1115/1.2137760).
- [30] Y. Peles, A. Koşar, C. Mishra, C.-J. Kuo, B. Schneider, Forced convective heat transfer across a pin fin micro heat sink, *International Journal of Heat and Mass Transfer* 48 (2005) 3615–3627, doi:[10.1016/j.jheatmasstransfer.2005.03.017](https://doi.org/10.1016/j.jheatmasstransfer.2005.03.017).
- [31] K.A. Moores, Y.K. Joshi, Effect of Tip Clearance on the Thermal and Hydrodynamic Performance of a Shrouded Pin Fin Array, *J. Heat Transfer* 125 (2003) 999, doi:[10.1115/1.1621897](https://doi.org/10.1115/1.1621897).
- [32] R.S. Prasher, J. Dirner, J.-Y. Chang, A. Myers, D. Chau, D. He, S. Prstic, Nusselt Number and Friction Factor of Staggered Arrays of Low Aspect Ratio Micro-Pin-Fins Under Cross Flow for Water as Fluid, 2006, p. 12.
- [33] A.M.S. Ho, W. Qu, F. Pfefferkorn, Pressure Drop and Heat Transfer in a Single-Phase Micro-Pin-Fin Heat Sink, in: *Heat Transfer*, Volume 3, ASME, Chicago, Illinois, USA, 2006, pp. 213–220, doi:[10.1115/IMECE2006-14777](https://doi.org/10.1115/IMECE2006-14777).
- [34] W. Qu, A. Siu-Ho, Liquid Single-Phase Flow in an Array of Micro-Pin-Fins—Part I: Heat Transfer Characteristics, *Journal of Heat Transfer* 130 (2008) 122402, doi:[10.1115/1.2970080](https://doi.org/10.1115/1.2970080).
- [35] W. Qu, A. Siu-Ho, Liquid Single-Phase Flow in an Array of Micro-Pin-Fins—Part II: Pressure Drop Characteristics, *Journal of Heat Transfer* 130 (2008) 124501, doi:[10.1115/1.2970082](https://doi.org/10.1115/1.2970082).
- [36] W. Qu, A. Siu-Ho, Measurement and prediction of pressure drop in a two-phase micro-pin-fin heat sink, *International Journal of Heat and Mass Transfer* 52 (2009) 5173–5184, doi:[10.1016/j.jheatmasstransfer.2009.05.007](https://doi.org/10.1016/j.jheatmasstransfer.2009.05.007).
- [37] W. Qu, A. Siu-Ho, Experimental study of saturated flow boiling heat transfer in an array of staggered micro-pin-fins, *International Journal of Heat and Mass Transfer* 52 (2009) 1853–1863, doi:[10.1016/j.jheatmasstransfer.2008.10.008](https://doi.org/10.1016/j.jheatmasstransfer.2008.10.008).
- [38] M. Liu, D. Liu, S. Xu, Y. Chen, Experimental study on liquid flow and heat transfer in micro square pin fin heat sink, *International Journal of Heat and Mass Transfer* 54 (2011) 5602–5611, doi:[10.1016/j.jheatmasstransfer.2011.07.013](https://doi.org/10.1016/j.jheatmasstransfer.2011.07.013).
- [39] C. Green, P. Kottke, X. Han, C. Woodrum, T. Sarvey, P. Asrar, X. Zhang, Y. Joshi, A. Fedorov, S. Sitarman, M. Bakir, A Review of Two-Phase Forced Cooling in Three-Dimensional Stacked Electronics: Technology Integration, *Journal of Electronic Packaging* 137 (2015) 040802, doi:[10.1115/1.4031481](https://doi.org/10.1115/1.4031481).
- [40] P. Asrar, X. Zhang, C.E. Green, M. Bakir, Y.K. Joshi, Flow boiling of R245fa in a microgap with staggered circular cylindrical pin fins, *International Journal of Heat and Mass Transfer* 121 (2018) 329–342, doi:[10.1016/j.jheatmasstransfer.2017.12.117](https://doi.org/10.1016/j.jheatmasstransfer.2017.12.117).
- [41] S.A. Isaacs, Y. Joshi, Y. Zhang, M.S. Bakir, Y.J. Kim, Two-Phase Flow and Heat Transfer in Pin-Fin Enhanced Micro-Gaps With Non-Uniform Heating, *ASME 2013 4th International Conference on Micro/Nanoscale Heat and Mass Transfer*, ASME, Hong Kong, China, 2013 V001T12A003, doi:[10.1115/MNHMT2013-22124](https://doi.org/10.1115/MNHMT2013-22124).
- [42] T.E. Sarvey, Y. Hu, C.E. Green, P.A. Kottke, D.C. Woodrum, Y.K. Joshi, A.G. Fedorov, S.K. Sitarman, M.S. Bakir, Integrated Circuit Cooling Using Heterogeneous Micropin-Fin Arrays for Nonuniform Power Maps, *IEEE Trans. Compon., Packag. Manufact. Technol.* 7 (2017) 1465–1475, doi:[10.1109/TCPMT.2017.2704525](https://doi.org/10.1109/TCPMT.2017.2704525).
- [43] T. İzci, M. Koz, A. Koşar, The Effect of Micro Pin-Fin Shape on Thermal and Hydraulic Performance of Micro Pin-Fin Heat Sinks, *Heat Transfer Engineering* 36 (2015) 1447–1457, doi:[10.1080/01457632.2015.1010921](https://doi.org/10.1080/01457632.2015.1010921).
- [44] E. Rasouli, C. Naderi, V. Narayanan, Pitch and aspect ratio effects on single-phase heat transfer through microscale pin fin heat sinks, *International Journal of Heat and Mass Transfer* 118 (2018) 416–428, doi:[10.1016/j.jheatmasstransfer.2017.10.105](https://doi.org/10.1016/j.jheatmasstransfer.2017.10.105).
- [45] Barry N. Taylor, Chris E. Kuyatt, Guidelines for evaluating and expressing the uncertainty of NIST measurement results, 1994.
- [46] D.L. Gee, R.L. Webb, Forced convection heat transfer in helically rib-roughened tubes, *International Journal of Heat and Mass Transfer* 23 (1980) 1127–1136, doi:[10.1016/0017-9310\(80\)90177-5](https://doi.org/10.1016/0017-9310(80)90177-5).
- [47] R.S. Prasher, J. Dirner, J.Y. Chang, A. Myers, D. Chau, D. He, S. Prstic, Nusselt number and friction factor of staggered arrays of low aspect ratio micropin-fins under cross flow for water as fluid, *J. Heat Transfer* 129 (2007) 141–153, doi:[10.1115/1.2402179](https://doi.org/10.1115/1.2402179).
- [48] T. İzci, M. Koz, A. Koşar, The effect of micro pin-fin shape on thermal and hydraulic performance of micro pin-fin heat sinks, *Heat Transf. Eng.* 36 (2015) 1447–1457, doi:[10.1080/01457632.2015.1010921](https://doi.org/10.1080/01457632.2015.1010921).
- [49] A. Mohammadi, A. Koşar, Hydrodynamic and Thermal Performance of Microchannels With Different Staggered Arrangements of Cylindrical Micro Pin Fins, *J. Heat Transfer* 139 (2017) 1–14, doi:[10.1115/1.4035655](https://doi.org/10.1115/1.4035655).
- [50] V. Saravanan, C.K. Umesh, D. Hiithaish, K. Seetharamu, Numerical investigation of pressure drop and heat transfer in pin fin heat sink and micro channel pin fin heat sink, *Int. J. Heat Technol.* 36 (2018) 267–276, doi:[10.18280/ijht.360136](https://doi.org/10.18280/ijht.360136).
- [51] R.K. Shah, A.L. London, Discussion—An Overview for the Designer and the Applied Mathematician, in: *Laminar Flow Forced Convection in Ducts*, Elsevier, 1978, pp. 385–420, doi:[10.1016/B978-0-12-020051-1.50022-X](https://doi.org/10.1016/B978-0-12-020051-1.50022-X).
- [52] R.K. Shah, A.L. London, Parallel Plates, in: *Laminar Flow Forced Convection in Ducts*, Elsevier, 1978, pp. 153–195, doi:[10.1016/B978-0-12-020051-1.50011-5](https://doi.org/10.1016/B978-0-12-020051-1.50011-5).
- [53] C.R. Kharangate, K. Wook Jung, S. Jung, D. Kong, J. Schaadt, M. Iyengar, C. Malone, H. Lee, M. Asheghi, K.E. Goodson, Experimental Investigation of Embedded Micropin-Fins for Single-Phase Heat Transfer and Pressure Drop, *Journal of Electronic Packaging* 140 (2018) 021001, doi:[10.1115/1.4039475](https://doi.org/10.1115/1.4039475).
- [54] D. Kong, K.W. Jung, S. Jung, D. Jung, J. Schaadt, M. Iyengar, C. Malone, C.R. Kharangate, M. Asheghi, K.E. Goodson, H. Lee, Single-phase thermal and hydraulic performance of embedded silicon micro-pin fin heat sinks using R245fa, *International Journal of Heat and Mass Transfer* 141 (2019) 145–155, doi:[10.1016/j.jheatmasstransfer.2019.05.073](https://doi.org/10.1016/j.jheatmasstransfer.2019.05.073).
- [55] R.S. Prasher, J. Dirner, J.-Y. Chang, A. Myers, D. Chau, D. He, S. Prstic, Nusselt Number and Friction Factor of Staggered Arrays of Low Aspect Ratio Micropin-Fins Under Cross Flow for Water as Fluid, *Journal of Heat Transfer* 129 (2007) 141, doi:[10.1115/1.2402179](https://doi.org/10.1115/1.2402179).
- [56] A. Kosar, Y. Peles, TCPT-2006-096.R2: Micro Scale pin fin Heat Sinks — Parametric Performance Evaluation Study, *IEEE Trans. Comp. Packag. Technol.* 30 (2007) 855–865, doi:[10.1109/TCAPT.2007.906334](https://doi.org/10.1109/TCAPT.2007.906334).
- [57] Z.G. Liu, H. Guan, C.W. Zhang, G.L. Jiang, The Flow Resistance and Heat Transfer Characteristics of Micro Pin-Fins with Different Cross-Sectional Shapes, *Nanoscale and Microscale Thermophysical Engineering* 19 (2015) 221–243, doi:[10.1080/15567265.2015.1073820](https://doi.org/10.1080/15567265.2015.1073820).
- [58] F. Xu, H. Wu, Experimental Study of Water Flow and Heat Transfer in Silicon Micro-Pin-Fin Heat Sinks, *Journal of Heat Transfer* 140 (2018) 122401, doi:[10.1115/1.4040956](https://doi.org/10.1115/1.4040956).
- [59] E. Rasouli, C. Naderi, V. Narayanan, Pitch and aspect ratio effects on single-phase heat transfer through microscale pin fin heat sinks, *International Journal of Heat and Mass Transfer* 118 (2018) 416–428, doi:[10.1016/j.jheatmasstransfer.2017.10.105](https://doi.org/10.1016/j.jheatmasstransfer.2017.10.105).
- [60] P.M. Nakod, S.V. Prabhu, R.P. Vedula, Heat transfer augmentation between impinging circular air jet and flat plate using finned surfaces and vortex generators, *Experimental Thermal and Fluid Science* 32 (2008) 1168–1187, doi:[10.1016/j.expthermflusci.2008.01.009](https://doi.org/10.1016/j.expthermflusci.2008.01.009).
- [61] Y. Wang, F. Houshmand, D. Elcock, Y. Peles, Convective heat transfer and mixing enhancement in a microchannel with a pillar, *International Journal of Heat and Mass Transfer* 62 (2013) 553–561, doi:[10.1016/j.jheatmasstransfer.2013.03.034](https://doi.org/10.1016/j.jheatmasstransfer.2013.03.034).

- [62] M.I. Hasan, Investigation of flow and heat transfer characteristics in micro pin fin heat sink with nanofluid, *Applied Thermal Engineering* 63 (2014) 598–607, doi:[10.1016/j.applthermaleng.2013.11.059](https://doi.org/10.1016/j.applthermaleng.2013.11.059).
- [63] P.A. Kottke, T.M. Yun, C.E. Green, Y.K. Joshi, A.G. Fedorov, Two-Phase Convective Cooling for Ultrahigh Power Dissipation in Microprocessors, *Journal of Heat Transfer* 138 (2016) 011501, doi:[10.1115/1.4031111](https://doi.org/10.1115/1.4031111).
- [64] G.A. Gabriele, K.M. Ragsdell, The Generalized Reduced Gradient Method: A Reliable Tool for Optimal Design, *ASME, J. Eng. Ind.* 99 (2) (May 1977) 394–400, doi:[10.1115/1.3439249](https://doi.org/10.1115/1.3439249).
- [65] Leon S. LASDON, et al., Design and testing of a generalized reduced gradient code for nonlinear programming, *ACM Transactions on Mathematical Software (TOMS)* 4 (1) (1978) 34–50.